ACS APPLIED MATERIALS & INTERFACES

Research Article

www.acsami.org

Self-Poled Transparent and Flexible UV Light-Emitting Cerium Complex–PVDF Composite: A High-Performance Nanogenerator

Samiran Garain,[†] Tridib Kumar Sinha,[‡,#] Prakriti Adhikary,[†] Karsten Henkel,[§] Shrabanee Sen,[∥] Shanker Ram,[⊥] Chittaranjan Sinha,[‡] Dieter Schmeißer,[§] and Dipankar Mandal*[,†]

[†]Organic Nano-Piezoelectric Device Laboratory, Department of Physics and [‡]Department of Chemistry, Inorganic Section, Jadavpur University, Kolkata 700032, India

[§]Angewandte Physik-Sensorik, Brandenburgische Technische Universität Cottbus-Senftenberg, K.-Wachsmann-Allee 17, 03046 Cottbus, Germany

[∥]Central Glass and Ceramic Research Institute (CSIR), 188 Raja S C Mullik Road, Kolkata 700032, India

[⊥]Materials Science Centre, Indian Institute of Technology (IIT), Kharagpur 721302, India

Supporting Information

ABSTRACT: Cerium(III)-*N*,*N*-dimethylformamide-bisulfate [$Ce(DMF)(HSO_4)_3$] complex is doped into poly(vinylidene fluoride) (PVDF) to induce a higher yield (99%) of the electroactive phases (β- and γ-phases) of PVDF. A remarkable enhancement of the output voltage (~32 V) of a nanogenerator (NG) based on a nonelectrically poled cerium(III) complex containing PVDF composite film is achieved by simple repeated human finger imparting, whereas neat PVDF does not show this kind of behavior. This high electrical output resembles the generation of self-poled electroactive β-phase in PVDF due to the electrostatic interactions between the fluoride of PVDF and the surface-active positive charge cloud of the cerium complex via H-bonding and/or bipolar interaction among the opposite poles of cerium complex and PVDF, respectively. The capacitor charging capability of the flexible NG promises its applicability as piezoelectric-based energy harvester. The cerium(III) complex doped PVDF composite film exhibit an intense photoluminescence in the UV region, which might be due to a participation of electron cloud from negative pole of bipolarized PVDF. This fact may open a new area for prospective development of high-performance energy-saving flexible solid-state UV light emitters.

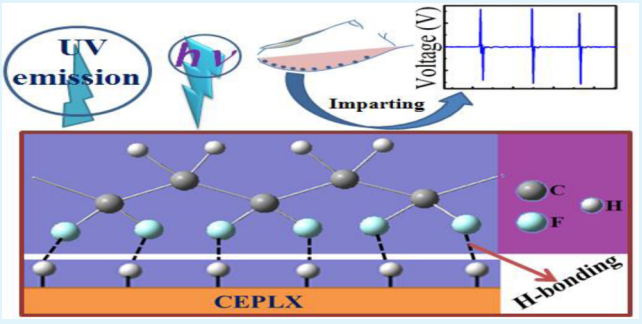

KEYWORDS: *PVDF, electroactive phase, nanogenerator, cerium charge transfer complex, piezoelectric energy harvester, UV-emitter*

INTRODUCTION

Electroactive polymers are among the most interesting classes of polymers utilized as smart materials in various applications, such as sensors, actuators, imaging systems, flash memories, energy harvesters, power storage materials, and functional biomaterials.[1−8] Poly(vinylidine fluoride) (PVDF) is one of the electoactive semicrystalline thermoplastic polymers that possess excellent flexibility, chemical resistance, tractability, and readily tunable properties.[2,9−13] Recently, the development of self-powering devices with electroactive PVDF films became a versatile technique where the realization of nanogenerator (NG) structures is most effective for energy-harvesting applications.[6,8,10] The tremendous growth of the portable electronic devices industry has resulted in the steady reduction of the operating voltages, sizes, and weights of electronic devices opening the possibility of self-powered electronic systems (where no batteries are required). Also, environmental monitoring, implantable biomedical devices, and wearable self-powered electronic devices are coming up to the market.[14−16] Since the past few decades, energy harvesting from environmental noise, friction, biomechanical, thermal, and low-frequency mechanical deformation has shown a huge impact on the energy sector.[17−19] Several research groups have attempted to fabricate high-performance NG by well-grown inorganic nanostructures and its composite forms with polymers. A variety of inorganic piezoelectric materials, namely, $BaTiO_3$, PZT, $ZnSnO_3$, ZnO, GaN, etc., have been potentially examined in diverse forms.[4,17,20−25] However, because of complicated and cost-intensive sophisticated synthesis, processability, and brittleness of these hazardous materials, the practical implementation of these materials for piezoelectric-based energy harvesters, especially in harsh environment, is limited. Thus, biocompatible flexible PVDF composites with easy preparation and cost-effective device fabrication are one of the best alternatives. However, to utilize PVDF for NG fabrication, the nucleation of the β ($TTTT$ conformation) and γ

Received: October 29, 2014
Accepted: December 19, 2014
Published: December 19, 2014

DOI: 10.1021/am507522r
ACS Appl. Mater. Interfaces 2015, 7, 1298−1307

($T_3GT_3\bar{G}$ conformation)-phases are in the focus of interest due to their polar electroactive conformations, whereas α ($TGTG$ conformation)-phase is electrically nonactive.[3] It is widely accepted that the electroactive phases in PVDF give raise to the ferroelectric behavior and exhibit piezoelectric as well as pyroelectric properties upon electrical poling.[10] Thus, the cost effectiveness of the film preparation aids its industrial viability to fabricate various types of smart sensors, nonvolatile ferroelectric memories, pressure and temperature sensitive electronics components, and embedded health monitoring textiles.[2,3,7,8] However, to induce the electroactive phases in PVDF either mechanical stretching or high electric field under controlled pressure are needed where the quality of the films and the yield of the batch production in industry are not up to the mark for device fabrication. To overcome this real-world problem associated with the nucleation of the electroactive β-phase in PVDF, the addition of external additives into the PVDF matrix became one of the good alternatives.

In this paper, we report a novel, flexible, paperlike, and lightweight organic–inorganic composite-based hybrid piezoelectric material using a rare earth metal (particularly, cerium) complex as inorganic counterpart in PVDF. Surprisingly, this PVDF-cerium complex composite film showed high performance of piezosensitivity under uniaxial pressure without any electrical poling. This result suggests that this composite film is a good candidate in real applications due to its easy fabrication and wide applicability in a large number of available vertical compression systems such as road transport, footpaths, bridges, vehicle tires, shoes, and many others. We chose the cerium complex (CEPLX) as additive to nucleate the electroactive β-phase in PVDF for large-scale production of flexible piezoelectric films with additional UV light-emitting capabilities. In addition, the versatile photophysical properties of cerium (+3/+4) ions have inspired vigorous research activities owing to a wide range of potential applications in the fields of bioassays, sensor systems, and optical materials.[26,27] Compared with other lanthanide ions, Ce^{3+} has the simplest $4f^n$ configuration ($n = 1$), and its broad band emission originating from parity-allowed interconfigurational $4f^05d^1 \rightarrow 4f^15d^0$ transitions is also studied for further understanding of d $\rightarrow$f luminescence processes.[29] We achieved a very high proportion of the piezoelectric β-phase in solvent-casted polymer composite film that also exhibits a very intense UV light emission. Furthermore, because of the readily variable ionic (+3/+4) states of cerium, it is also expected that cerium complex containing PVDF (CEPLX–PVF_2) films may promote versatile applications such as chemical sensors and catalysts as well.[30] To explain the high yield of self-poled piezoelectric β-phase a special emphasis has been put on the investigation of the plausible role of hydrogen bonding and the electrostatic interaction, which may happen between the surface-active positive charge cloud (proton generated in the vicinity of outer surface of cerium complex) and the induced negative pole of the polymer chain. The induced dipole in PVDF matrixes may interact with each other through intermolecular H-bonding between the opposite poles of the consecutive matrixes. Thus, there is a chance of generation of β-phase as well as H-bond induced self-poling.[31] A CEPLX on the other hand may be treated as a combination of dipole as a whole.[32] So, there will be a bipolar interaction among the opposite poles of CEPLX and PVDF, respectively.[33] This type of interaction may promote the generation of the electroactive β-phase in PVDF and self-poling as well. The composite now can be imagined as a non-cetrosymmetric CEPLX encapsulated in β-phase generated PVDF matrixes in layer-by-layer pattern. The CEPLX having different bulky ligands (i.e., DMF and $-HSO_4$) will repel each other and form a non-centrosymmetric complex and thus may exhibit piezoelectricity.[34] So the complexes encapsulated in crystalline (β-phase) PVDF matrixes via electrostatic interactions (like H-bonding) may be treated overall as composite of giant crystal-like structures. We hypothesize that this interaction and the overall deformation of the composite crystal during the application of external uniaxial pressure led to the induction of an electric potential difference between the top and bottom surfaces of the composite film. Thus, an enhanced piezoelectric response is observed. Thus, the combination of the piezoelectric properties of PVDF with the functionality added by the CEPLX may open the usability of CEPLX–PVF_2 films in a wide range of applications.

EXPERIMENTAL SECTION

Materials. Poly(vinylidene fluoride) (PVDF) pellets ($\bar{M}_w \approx$ 275 000, Sigma-Aldrich, USA), *N*,*N*-dimethylformamide (DMF, Merk Chemical, India), and ammonium cerium sulfate dihydrate (CESLT) ($(NH_4)_4Ce(SO_4)_4{\cdot}2H_2O$, Alpha-Aesar, USA).

Preparation of CEPLX–PVF_2 Films. Different wt (w/v) % (i.e., 0.06, 0.12, 0.25, 0.50, 1.0) aliquots of CESLT were added into the PVDF–DMF solutions, and the resulting solutions were stirred at 60 °C until its color changed from pale yellow to milky white (Supporting Information, Figure S1). The solutions were cast on clean glass substrates and dried at 120 °C for 5 h, and finally the films (CEPLX–PVF_2) were peeled from the substrates for characterization and device fabrication. The CEPLX–PVF_2 films are named as CEPLX#–PVF_2, where # stands for the wt % of the CESLT within the PVDF–DMF solution. Furthermore, note that we also performed a control experiment by adding the desirable amount of CESLT in DMF (without PVDF) and keeping the solution at 60 °C under stirring until white precipitation (CEPLX) was obtained. Finally CEPLX was dried at 120 °C and proceeded for characterization. A neat PVDF–DMF solution was also used to prepare a reference sample in similar way, designated as PVF_2.

Characterization. The crystalline phases of PVDF were identified by Fourier transform infrared spectroscopy (FT-IR) (Shimadzu, FTIR-8400S) results. The X-ray photoelectron spectroscopy (XPS) was performed by an instrument equipped with a Mg Kα X-ray source and a semispherical electron analyzer made by Leybold–Heraeus. To investigate the degree of crystallinity, X-ray diffraction (XRD) analysis was carried out with a Bruker, D8 Advance, X-ray diffractometer, operated at 40 kV and 40 mA with Cu Kα radiation (λ = 1.54 Å). The morphology of the films was studied with a field emission scanning electron microscope (FE-SEM, INSPECT F50) operated at an acceleration voltage of 20 kV. The chemical composition was traced with energy-dispersive X-ray spectroscopy (EDS) and recorded with Bruker Nano X-flash detector (410-M) equipped with FE-SEM chamber. UV–vis spectra (Shimadzu, 3110PC) were recorded for analyzing the optical quality of the CEPLX–PVF_2 films. Photoluminescence (PL) spectra were recorded with Horiba (iHR320) luminescence spectrometer with an excitation wavelength (λ_{ex}) of 270 nm. NGs were fabricated by simply pasting carbon tape as electrodes onto both sides of the CEPLX–PVF_2 films. Human finger touch responses were recorded in terms of open-circuit output voltage using a digital storage oscilloscope (Agilent, DSO3102A). The typical circuit diagram is shown in Supporting Information, Figure S11. The capacitor charging performance was employed via a typical rectifier bridge circuit. All measurements were carried out at room temperature.

RESULTS AND DISCUSSION

Crystallographic Phase Identification. The neat PVDF film (sample: PVF_2) contains predominantly α-phase characteristic peaks (shown in Figure 1i) attributed to the FT-IR

DOI: 10.1021/am507522r
ACS Appl. Mater. Interfaces 2015, 7, 1298–1307

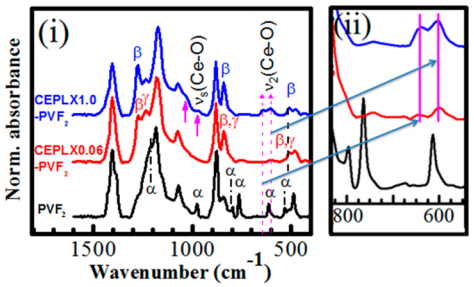

Figure 1. (i) FT-IR spectra of PVF_2 and CEPLX−PVF_2 films in the wavenumber region from 1600 to 400 cm^{-1}. (ii) Enlarged spectra in the range from 825 to 550 cm^{-1} for the discussion of the appearance of additional peaks at 640 and 602 cm^{-1} due to cerium coordination complex formation.

absorbance bands at 1212, 976, 764, 614, and 532 cm^{-1}.[11,12,35] In contrast, all these bands are completely diminished in the spectra of the CEPLX0.06−PVF_2 and CEPLX1.0−PVF_2 films, indicating new phase formations, namely, β-and γ-phases. The piezoelectric β-phase ($TTTT$) can be well-identified from the peak at 1276 cm^{-1}, whereas the semipolar γ-phase ($TTTG$) is evident from the peak at 1236 cm^{-1}.[11,12,35] In addition, the β- and γ-phases resemble each other structurally and spectroscopically due to the existence of TTT in the chain conformation in both γ-and β-phases giving rise to some common vibrational bands such as at 841 and 510 cm^{-1}.[2,11,35]

It is interesting to note that a very small amount (0.06 wt %) of CESLT can hinder the α-phase nucleation and preferentially induce the polar β- and γ- phases. The relatively intense absorption at 1236 cm^{-1}, in comparison with 1276 cm^{-1} band, indicates that the CEPLX0.06−PVF_2 film exhibits a relatively higher proportion of the γ-phase compared to the β-phase. However, at higher CESLT concentration (Supporting Information, Figures S2 and S3), the β-phase is significantly improved as revealed from the 1276 cm^{-1} band intensity of the CEPLX1.0−PVF_2 film, and subsequently its γ-phase (1236 cm^{-1}) band intensity is diminished. This information is further supported by Figure S3, where the band intensities responsible for α-, β-, and γ-phases are plotted as a function of the CESLT concentration. The two additional well-resolved peaks at 640 and 602 cm^{-1} shown in Figure 1ii signify the cerium-coordinate complex formation (Supporting Information, Figure S5 and Scheme S1). Two other arrow-marked broad peaks at 1041 and 972 cm^{-1} (Figure 1i) are also evidencing that cerium-coordinate complex formation is increased when the CESLT concentration is higher. Note also that the dependence of the β-phase intensity (1276 cm^{-1} band) on the CESLT concentration is similar to that of the 640 cm^{-1} band (as shown in Figure 1ii) revealing that these bands are correlated.

To perform a qualitative analysis of the α-, β-, and γ-phases, the changes of the absorption intensities of the α- (764 cm^{-1}), β- (1276 cm^{-1}), and γ-phases (1236 cm^{-1}) are plotted as a function of the CESLT content (Supporting Information, Figure S3). With the increase of the CESLT content the α-phase fraction is gradually decreased, whereas the β-phase part is gradually increased. An abrupt increase of the β- and γ-phases in the CESLT content range of 0.06−0.12 wt % is observed; hereafter, the γ-phase content is decreasing gradually. The strong absorption band at 841 cm^{-1} appeared in CEPLX−PVF_2 films (Figure 1i) is reflecting a common characteristic of both electroactive β- and γ-phases.[2,9,36] For a system containing α-, β-, and γ-phases the relative electroactive phase fraction (F_{EA} including β- and γ-phases) can be calculated using the following equation.

$$F_{EA} = \frac{A_{EA}}{\left(\frac{K_{841}}{K_{764}}\right)A_{764} + A_{EA}} \times 100\% \quad (1)$$

where A_{EA} and A_{764} are the absorbance intensities at 841 and 764 cm^{-1}, respectively, and K_{841} (7.7×10^4 cm^2 mol^{-1}) and K_{764} (6.1×10^4 cm^2 mol^{-1}) are the absorption coefficients at the respective wavenumbers.[2]

The variation of F_{EA} with increasing amount of CESLT concentration is presented in Supporting Information, Figure S7. An F_{EA} value of 94% is achieved at very small amount of CESLT (0.06 wt %), and then it stays nearly stable with further increasing of CESLT concentration and approaches 99% for the CEPLX1.0−PVF_2 film. The vibration band at 764 cm^{-1} (α-phase) disappeared (see also Figure S2) by the addition of CESLT, and a new broad peak is observed at 3230 cm^{-1} (Supportilng Information, Figure S8), which is corresponding to O−H stretching modes.[37] In previous reports, H-bonds are responsible for the electroactive β-phase nucleation in hydrated salt-added PVDF film.[13,37] Thus, at the interface between the $-HSO_4$ and PVDF, the $-HSO_4$ ligand molecules may form hydrogen bonds with adjacent PVDF chains as illustrated in Figure 2a. These bonds may result in the readjustment of fluorine atoms to a certain extent, and bring more trans conformation into the polymer chain. To provide evidence for the explanation given above, the FT-IR spectra of the PVDF films with different concentrations of CESLT were compared within the 3400−2800 cm^{-1} region, as shown in Figure S8. For the PVDF film without CESLT (i.e., PVF_2) there are no observable peaks in the range of 3400−3100 cm^{-1}, while the CEPLX-containing films present a broad band with a peak centered at 3230 cm^{-1}. It becomes stronger with the increase of the CESLT concentration (see also inset of Figure 2f). We believe that the band at 3230 cm^{-1} corresponds to OH groups bonded via hydrogen bond with fluorine atoms (O−H···F−C, see Figure 2a). The nature of the surface environment within the CEPLX1.0−PVF_2 film was explored by high-resolution S 2p and O 1s XPS spectra (Figure 2e), which exhibit broad peaks at 169.5 and 531.5 eV, respectively, consistent with a unique HSO_4^- environment. The deconvoluted peak of S 2p core level spectrum is composed of two overlapping peaks centered at 169.3 and 170.4 eV, which corresponds to the $S(2p_{3/2})$ and $S(2p_{1/2})$ spin−orbit states, respectively, where sulfur in the CEPLX1.0−PVF_2 film exists in hexavalent oxidation state (S^{6+}). The 531.1 eV peak is attributed to the presence of a S−O−Ce linkage, and 532.1 eV could be due to S−O bonds and OH groups as revealed from O 1s core level deconvoluted spectrum.

At the highest CESLT concentration (i.e.,1 wt %), the FT-IR absorption band at 3230 cm^{-1} is much stronger than at the lowest concentration (0.06 wt %) indicating that distinctly more OH groups of $-HSO_4$ that formed hydrogen bonds with PVDF exist in the CEPLX1.0−PVF_2 film, as shown in the inset of Figure 2d. In addition, the oxygen atoms of $-HSO_4$ may also form H-bonds with PVDF. This is further clarified by the ratio of the absorption peak intensities of the CEPLX−PVF_2 films to the neat PVDF film (i.e, $A_{CEPLX-PVF2}/A_{PVF2}$) at 3220 cm^{-1}; obviously, it progresses monotonically with increasing CESLT concentration (Figure 2f). In contrast, the relative F_{EA} saturated already after the addition of a small amount of 0.06 wt % of CESLT (Figure S7). This indicates that some additional factors (others than H-bonding) are involved in the stabilization and

DOI: 10.1021/am507522r
ACS Appl. Mater. Interfaces 2015, 7, 1298−1307

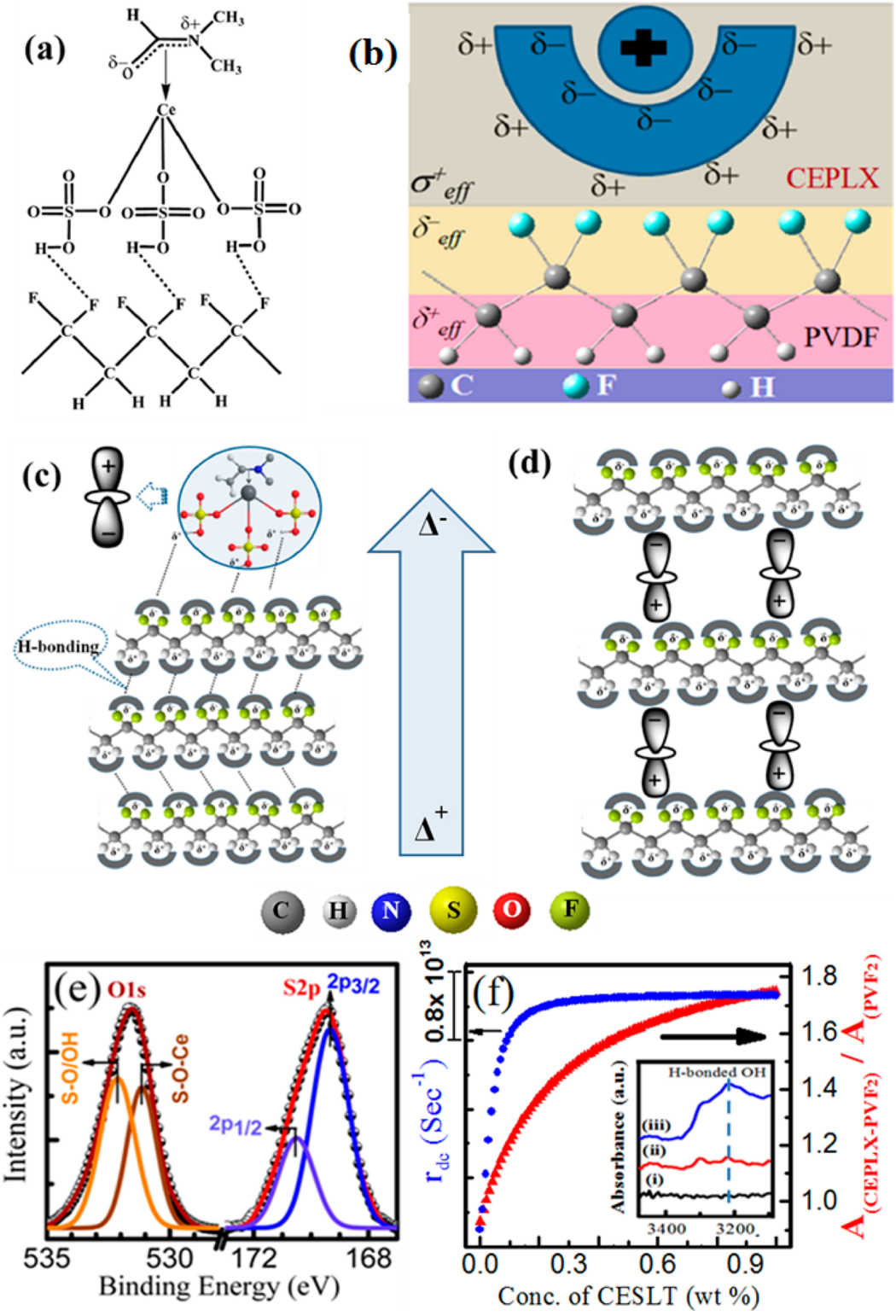

Figure 2. Schematic representation of (a) the formation of H-bonding with $-HSO_4$ and CF_2 dipoles and (b) the electrostatic interaction between the surface charges of the CEPLX and the CF_2 dipoles. Self-poling due to (c) formation of intermolecular H-bonding and (d) dipolar interaction between opposite poles of the CEPLX and PVF_2. (e) Deconvoluted XPS spectra of O 1s and S 2p core levels of CEPLX1.0–PVF_2. (f) Variation of damping coefficient r_{dc} (left *y*-axis) and the absorbance intensity ratio of CEPLX–PVF_2 and neat PVF_2 film at 3230 cm^{-1} (right *y*-axis) with the CESLT loading in the polymer films. The inset of Figure 2f shows the FT-IR spectra of (i) PVF_2, (ii) CEPLX0.06–PVF_2, and (iii) CEPLX1.0–PVF_2 films in the region of 3500–3100 cm^{-1}.

improvement of the electroactive *β*- and *γ*-phases. Another reason behind the *β*-phase nucleation beside H-bonding may be governed by the electrostatic interaction between the surface-active positive charge cloud of the CEPLX and the CH_2/CF_2 dipoles of the PVDF chains as indicated in Figure 2a,b, or it might be due to the bipolar interaction between the opposite

DOI: 10.1021/am507522r
ACS Appl. Mater. Interfaces 2015, 7, 1298–1307

poles of CEPLX and PVDF (Figure 2d). The H-bonding interaction of PVDF with the surface active positive charge cloud of CEPLX can also influence the PVDF moieties to be arranged in layer-by-layer configuration via the intermolecular H-bonding as depicted in Figure 2c. These types of electrostatic interactions are also the key factor of self-poling. As the surface charge density (σ_{eff}) of the CEPLX carries positive sign, the CF_2 dipoles (δ^-_{eff}) of PVDF may interact when the surface of the complex is surrounded by a majority of positive charges (σ^+_{eff}).[36] The strong interaction between the electronegative CF_2 bonds of the PVDF chains and the positively charged surface of the CEPLX forces the polymer chains to align on the surface of the CEPLX in an extended *TTTT* conformation resulting in the formation of the β-PVDF crystallographic phase. This model is quite consistent with the FT-IR results shown in Figure S8 where a clear shifting of the CH_2 asymmetric (ν_{as}) and symmetric (ν_s) stretching vibrational bands toward the lower-frequency (wavenumber) side is evident in CEPLX-doped PVDF films with respect to the PVF_2 film, which affirms the electrostatic interaction model. The interfacial electrostatic interactions result in a damping of the oscillations of the CH_2 dipoles and correspondingly support the aforementioned shifts in the vibrational FT-IR bands. Here, we calculated the damping coefficient (r_{dc}) using the following equation.[6]

$$r_{dc} = 4\pi c(\overline{\nu}_{PVF_2}{}^2 - \overline{\nu}_{CEPLX-PVF2}{}^2)^{1/2} \quad (2)$$

where c is the velocity of light and $\overline{\nu}_{PVF_2}{}^2$ and $\overline{\nu}_{CEPLX-PVF2}{}^2$ are the wavenumbers of the damping free oscillation of the CH_2 groups of the PVF_2 and damping containing CEPLX–PVF_2 samples, respectively. The variation of r_{dc} with the CESLT loading (Figure 2f) indicates that the r_{dc} increases with increasing salt concentration up to 0.3 wt % (percolation limit), and then it gets saturated.

Next, we discuss XRD data of the investigated films to confirm the findings of the FT-IR analysis.

The PVF_2 film exhibits XRD peaks at 17.6°(100), 18.2°(202), 19.7°(110), 26.2°(021), and a shoulder at 25.4° (120) (Figure 3c), which are characteristic for α-crystalline.[11] Thus, the PVF_2 film consists of predominantly α-crystalline phase, which is consistent with the FT-IR spectra shown in Figure 1i. In the CEPLX–PVF_2 films (samples: CEPLX0.06–PVF_2 and CEPLX1.0–PVF_2), the α-characteristic diffractions diminished, whereas few new peaks (i.e., at 18.5°, 20.2°) appeared (Figure 3a,b). The diffraction peaks at 18.5° (202) and 20.2° (110) in CEPLX0.06–PVF_2 are attributing the presence of the γ-phase with the coexistence of the β-phase as revealed from its broad diffraction peak at 20.5° (110/200). In the CEPLX1.0–PVF_2 film the β-phase content became more dominant as deduced from the intense diffraction peak at 20.5° and the reduction of the intensity of the γ-phase characteristic peak (at 18.5°).

Note that in the XRD pattern of the CEPLX1.0–PVF_2 film (Figure 3a) additional sharp diffraction peaks (marked with *) appear due to the presence of the inorganic CEPLX filler component within the PVDF matrix. Thus, the multiple sharp crystalline peaks signify that the cerium exists in a complex form within the PVDF matrix. The total degree of the crystallinity (χ_{c_t}) is calculated by curve deconvolution methodology using eq 3:

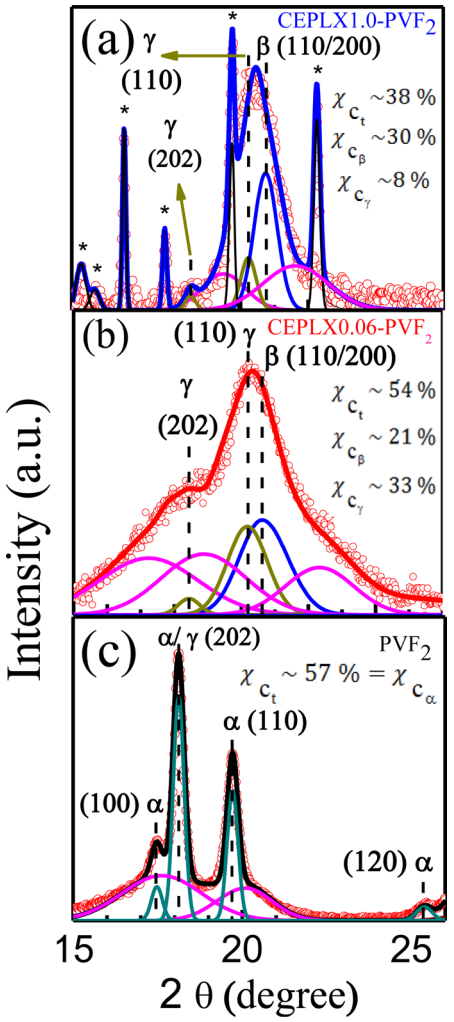

Figure 3. XRD patterns and their curve deconvolution of (a) CEPLX1.0–PVF_2, (b) CEPLX0.06–PVF_2, and (c) PVF_2 films. The dotted points are experimental data, and the solid lines correspond to the best curve fit. The crystallographic information is labeled, where χ_{c_t}, χ_{c_β}, χ_{c_γ}, χ_{c_α} represents the total, β-, γ-, and α-crystallinity. The peaks marked with * correspond to the CEPLX filler.

$$\chi_{c_t} = \frac{\sum A_{cr}}{\sum A_{cr} + \sum A_{amr}} \times 100\% \quad (3)$$

where ΣA_{cr} and ΣA_{amr} are the summation of the integral area of the crystalline peaks and the amorphous halo from PVDF, respectively.[9] It points out that χ_{c_t} (as labeled in Figure 3) is gradually reducing when the filler content is increasing, which is a general trend in polymer science happening due to inhibition of the tailoribility through the entanglement of the polymer matrix.[38-40] Thus, the CEPLX is retarding the crystallization of PVDF and favoring the amorphous structure in the PVDF and CEPLX composite films, which reduces the degree of crystallinity. Therefore, CEPLX–PVF_2 might be promising as a superior dielectric material.[41] The degrees of β-crystallinity (χ_{c_β}) and γ-crystallinity (χ_{c_γ}) are calculated by the following equations:

$$\chi_{c_\beta} = \chi_{c_t} \times \frac{\sum A_\beta}{\sum A_\beta + \sum A_\gamma}\% \quad (4)$$

DOI: 10.1021/am507522r
ACS Appl. Mater. Interfaces 2015, 7, 1298–1307

$$\chi_{c_\gamma} = \chi_{c_t} \times \frac{\sum A_\gamma}{\sum A_\beta + \sum A_\gamma}\% \quad (5)$$

where $\sum A_\beta$ and $\sum A_\gamma$ indicate the total integral area from β- and γ-crystalline phase peaks, respectively. By this analysis it was also found that the resulting content of the piezoelectric β-phase is higher (i.e., $\chi_{c_\beta} \approx 30\%$) in the CEPLX1.0−$PVF_2$ film although χ_{c_t} is relatively lower than it is in the CEPLX0.06−PVF_2 film. Therefore, it is expected that the CEPLX1.0−PVF_2 film should give better piezoresponse, as it is directly proportional to the β-crystallinity.

Surface Morphology. The photographs of the CEPLX−PVF_2 films in Figure 4a,b indicate that the CEPLX−PVF_2 films are completely flexible (see the video file V1) promising their applicability as lightweight flexible sensors.

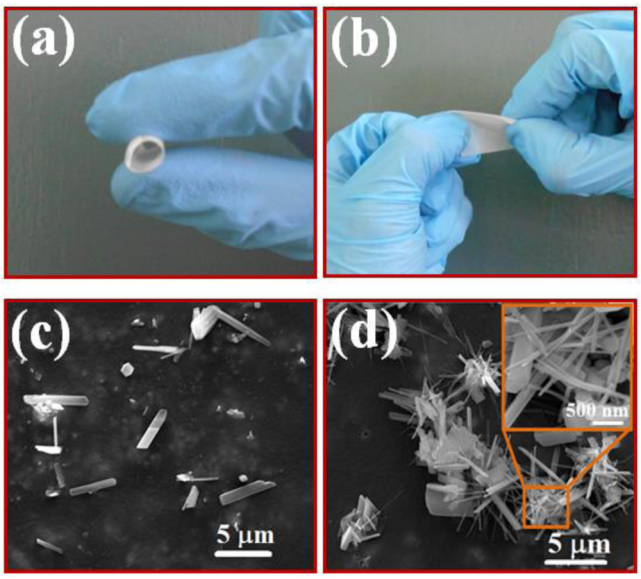

Figure 4. Digital photographs of the CEPLX1.0−PVF_2 film, demonstrating the flexibility in different ways, such as (a) rolling (b) twisting. FE-SEM images of (c) CEPLX0.06−PVF_2 and (d) CEPLX1.0−PVF_2 films. (inset) A higher-resolution image.

The surface morphology of the CEPLX−PVF_2 films (see Figure 4) showed distinct differences based on the CESLT concentration, and the typical fibril-like structures (a feature of the α-phase, which is usually observed in neat PVDF film, Figure S9, Supporting Information) are completely diminished. Thus, it signifies that the addition of CESLT (giving rise to CEPLX, as shown in Scheme S1, Supporting Information) can hinder the growth of the nonpolar α-phase and favors the electroactive phases in PVDF film. A large number of particles with different shapes and sizes are formed in CEPLX−PVF_2 films as observed in the FE-SEM micrographs (Figure 4c,d). The homogeneous dispersion of the rod-shaped particles is better in the CEPLX0.06−PVF_2 film as shown in Figure 4c. It might be due to the prevention of the aggregation of cerium comprising particles by the PVDF polymer host matrix. With the increase of the CESLT concentration, selective residual growths of relatively larger particles happened, as observed in the FE-SEM image of the CEPLX1.0−PVF_2 film (Figure 4d). Thus, it is also self-evident that the shape and size of the particles can be tuned by simply changing the concentration of the CESLT within the PVDF matrix.

The presence of chemical elements was further evidenced from EDS study (Supporting Information, Figure S10). The presence of C and F from PVDF and Ce, S, O, and N due to CEPLX formation was well-detected in the EDS spectra.

Optical Properties. To study the optical properties, UV−vis absorption and PL spectroscopy were performed on the CEPLX−PVF_2 films and on a pure CEPLX pellet where any influence of the PVDF matrix was excluded. The UV−vis spectra of the CEPLX−PVF_2 films (Figure 5a) indicate that the

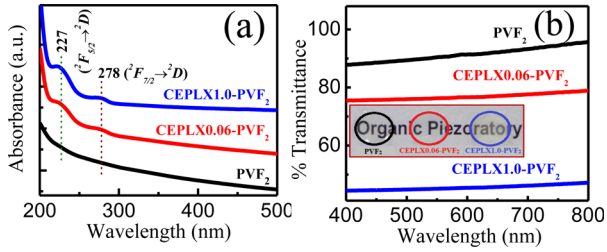

Figure 5. (a) UV−vis absorbance spectra and (b) transmittance spectra (covering the visible region) of PVF_2 and CEPLX−PVF_2 films. (inset) The digital photographs.

absorbance in the UV region was further improved in comparison to the PVF_2 film. Although the PVDF film itself creates the place to be used as a UV protective layer, the CEPLX−PVF_2 films may improve the degree of UV resistance capability as well. The transmittance spectra of the films (Figure 5b) and corresponding digital photographs (inset of Figure 5b) indicate that the visible transparency was not remarkably reduced even in higher proportion of the filler content. Furthermore, two broad bands appeared at ∼278 and 227 nm as labeled in Figure 5a, indicating the presence of Ce^{3+} ionic states and their conversion from Ce^{4+} ionic states.[28] These two UV absorption bands originating from $4f^1\ 5d^0 \rightarrow 4f^0\ 5d^1$ transitions of the Ce^{3+} ions are denoted as $^2F_{7/2} \rightarrow {}^2D$ and $^2F_{5/2} \rightarrow {}^2D$.[42] Note that, because of the ligands occupied by Ce^{3+} ion, the 4f ground electronic configuration splits into two states $^2F_{5/2}$ and $^2F_{7/2}$ resulting in $^2F_{5/2} \rightarrow {}^2D$ and $^2F_{7/2} \rightarrow {}^2D$ transitions, which are responsible for the peaks at 227 and 278 nm, respectively.

The PL spectra of the CEPLX pellet and CEPLX−PVF_2 films (Figure 6a−c) were recorded using an excitation wavelength of 270 nm. It is expected that the electron-donating ability of the lower valence ions is responsible for the 4f−5d excitation, while the electron acceptance of higher valence ions gives rise to charge-transfer transition from the host ligands to the rare-earth ion.

However, Ce^{3+} ions have only one electron in their 4f shell, which can be excited to the 5d orbitals upon UV light irradiation. Affected by the crystal field, the excited 5d state of Ce^{3+} splits into two spin−orbit components, designated as $^2D_{5/2}$ and $^2D_{3/2}$ as shown in Figure 6f.[43] Ce^{3+} coordinated with ligands matrix exhibits the excitation at 270 nm corresponding to transitions from the ground $^2F_{7/2}$ state to excited 5d states of the Ce^{3+} ions with consequent PL maxima at 320 and 341 nm (Figure 6a). In the complex structure, Ce^{3+} emission shows two bands due to the double character of the $4f^1$ ground state (spin−orbit components are $^2F_{5/2}$ and $^2F_{7/2}$ states), which are attributed to the $^2D \rightarrow {}^2F_{5/2}$ (320 nm) and $^2D \rightarrow {}^2F_{7/2}$ (341 nm) transitions.[44] These transitions are clearly shown by curve

DOI: 10.1021/am507522r
ACS Appl. Mater. Interfaces 2015, 7, 1298−1307

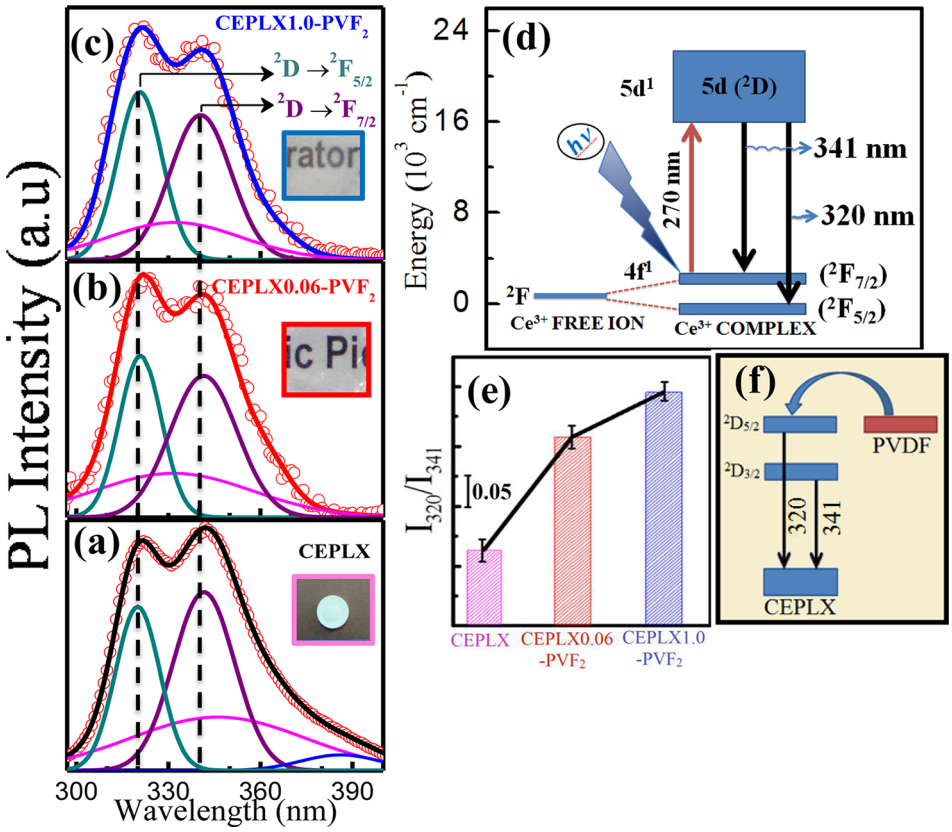

Figure 6. Room-temperature PL spectra of (a) CEPLX pellet and (b) CEPLX0.06−PVF_2 and (c) CEPLX1.0−PVF_2films (the photograph of the samples are displayed in the inset). The scattered points are experimental data, and the solid lines depict the curve deconvolution. (d) Energy-level diagram explaining the light emission from Ce^{3+} complex with excitation at λ_{ex} = 270 nm. (e) PL intensity ratio of the two peaks (I_{320}/I_{341}), (f) electron transition from PVDF to CEPLX.

deconvolution method resulting in two Gaussian peaks with maxima at 320 and 341 nm, respectively (Figure 6a). These results also indicate that two kinds of Ce^{3+} PL centers exist due to different coordination sites occupied by Ce^{3+} ions in the complex. The energy difference between these two transition bands is close to 2000 cm^{-1}, in good agreement with the characteristic splitting of the two Ce^{3+} 4f ground levels $^2F_{5/2}$ and $^2F_{7/2}$ induced by spin−orbit interaction.[45,46] The corresponding absorption (shown in Figure 5a) is also appearing in the UV spectral region. Accordingly, we can confirm that Ce^{4+} is reduced by DMF followed by Ce^{3+} complex formation where DMF also acts as a ligand. The luminescence intensity of the 320 nm band is weaker than that of the 341 nm band in the CEPLX sample, whereas in the CEPLX-containing PVDF films the intensity of 341 nm band is relatively lower when compared to the 320 nm band (Figure 6b,c). The PL intensity ratio of these two peaks, that is, I_{320}/I_{341}, supports this statement. It might be due to the H-bonding interaction between the ligand and the electronegative atom of PVDF, where a flow of an electron cloud from PVDF matrix toward the ^2D level of Ce^{3+} state may take place. A corresponding PL scheme in CEPLX−PVF_2 is depicted in Figure 6f, where the electron sharing from PVDF to CEPLX is illustrated.

Piezoresponse from NGs Made with CEPLX−PVF_2 Films. To investigate the piezoresponse of CEPLX−PVF_2 films, electrode-polymer-electrode (EPE) stacks (electrode area: 1.5 cm × 2.5 cm) were prepared, and the piezoresponse (open-circuit voltage across the top and bottom electrode) was detected directly by a digital oscilloscope (DSO). Results are shown in Figure 7, where repeated human finger imparting was applied onto the top surface as described in ref 9.

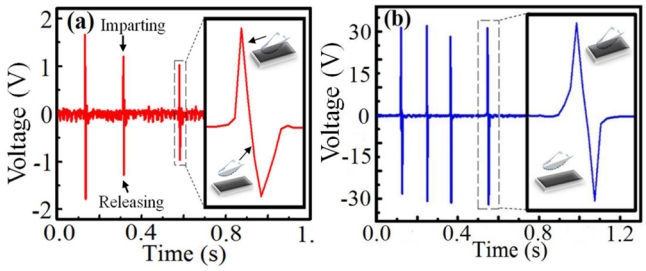

Figure 7. Piezoresponses from NGs made with CEPLX−PVF_2 films. The relatively lower output voltage is observed in the (a) CEPLX0.06−PVF_2 film, whereas a considerably higher voltage is found in the (b) CEPLX1.0−PVF_2 film.

Positive and negative amplitudes of the open-circuit voltage corresponding to finger imparting and releasing are observed as illustrated in Figure 7a. When human finger was imparting the top surface of the EPE stack-based NG charge distribution within the overall crystal structure comprising the CEPLX and the electroactive counterpart of PVDF film, charging occurred, leading to the generation of an electric potential difference between the two electrodes of the CEPLX−PVF_2 film and the corresponding open-circuit voltage, showing an amplitude with positive sign. Peaks with negative signs were observed when the

DOI: 10.1021/am507522r
ACS Appl. Mater. Interfaces 2015, 7, 1298−1307

finger was released. The open-circuit voltage of the CEPLX1.0–PVF_2 films reached 32 V, whereas only 1.8 V was observed for the CEPLX0.06–PVF_2 film. The proposed working mechanism of the hybrid composite CEPLX–PVF_2 films is a combined effect of the electroactivity of PVDF and CEPLX. The enhanced piezoresponse of the electroactive phase-dominated PVDF films are combined due to the change in dipole moment of PVDF itself with application of pressure along with the change in dipole moment of the non-centrosymmetric CEPLX attached to PVDF via electrostatic interaction/H-bonding.[31,47] The non-centrosymmetry of the CEPLX due to the steric repulsion between the bulky groups is assumed from its high piezoresponse. Thus, the deformation of the overall crystal structures in CEPLX–PVF_2 film causes the strong enhancement in piezoresponse (with efficient repeatability for multiple uses) only by the interchange of its deformed structure to stable one and vice versa with the application of external pressure. The positively charged cloud generated on the CEPLX surfaces actively interacts with the CF_2 part of CF_2/CH_2 dipoles of PVDF (Figure 2b) and promotes the formation of piezoelectric β-phase by surface charge induced polarization resulting in self-polarized films.[10] In addition, the applied external pressure builds a potential, which further supports the alignment of the electric dipoles of PVDF along the unidirection via stress-induced polarization.[48] Finally, the dipoles of PVDF molecules are self-polarized along a single direction due to stress and surface charge induced polarization without external electric field and result in a self-poled transparent and flexible PVDF nanogenarator. Under finger imparting, the CEPLX–PVF_2 layer experiences a strain over its surface, which produces a deformation in its crystal structure comprised of CEPLX and PVDF, leading to the generation of a piezopotential across the surface and finally to an electrical output signal. The high performance of the CEPLX–PVF_2 composite films provides a new platform for harvesting vibrationally bared energy available in surroundings. Besides instantaneous output voltage, the charging ability of the CEPLX–PVF_2 films was also tested with rectifier bridge circuit (Figure 8a), and the results are shown in Figure 8b,c. The

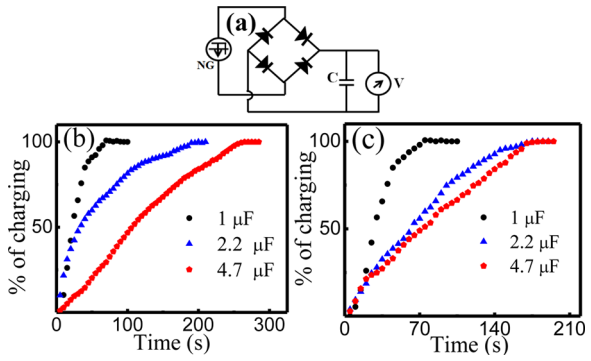

Figure 8. (a) Equivalent circuit diagram for capacitor charging with NGs. Charging response of different capacitors when being charged by the (b) CEPLX0.06–PVF_2 and (c) CEPLX1.0–PVF_2 film-based NG.

results indicate that the generated voltage of the CEPLX–PVF_2 film-based NGs is rectified to exponentially charge capacitors (specifically, 1, 2.2, and 4.7 μF) reaching finally the steady state. The NG based on the CEPLX0.06–PVF_2 film showed the 100% charging (steady state) after 288 s for the 4.7 μF capacitor (Figure 8a), while in the CEPLX1.0–PVF_2 film containing stack it was achieved after 192 s (Figure 8b). Likewise, for the other two capacitors (1 and 2.2 μF) the steady states were also reached within shorter times for the NG with CEPLX1.0–PVF_2 film in comparison to the NG with CEPLX0.06–PVF_2 film. It should be mentioned that the different charging abilities of the two NG with CEPLX–PVF_2 films are apparently determined by the amplitude of the generated output voltage of the films. Thus, the CEPLX1.0–PVF_2 film-based NG demonstrates adequate charging ability promising piezoelectric-based energy harvesting ability, which can be used directly to charge batteries of portable electronic components or for self-powering devices.

CONCLUSION

We have successfully performed the in situ synthesis of Ce(III) complex and its doping into PVDF. We achieved 99% yield of the electroactive phase within the transparent and flexible Ce(III) complex containing PVDF (CEPLX–PVF_2) composite films as revealed by FT-IR and XRD investigations. The results suggest that in the composite films electrostatic interactions (like H-bonding) between the Ce complex and the CF_2 groups of PVDF can lead to meaningful piezoelectric response. For the NG made with CEPLX–PVDF composite film an open-circuit output voltage up to 32 V was demonstrated, and its charging capability of capacitors reflects its potential to be used as piezoelectric-based energy harvesters where the traditional electrical poling of PVDF can be avoided.

The observed PL of the transparent and flexible composite films in the UV region is another proof of the existence of the Ce(III) complex within the PVDF matrix and the sharing of electrons from PVDF into the Ce (III) complex. The PL study confirms the possibility of using CEPLX–PVF_2 films in addition to their piezoresponse as flexible UV light-emitting materials, implying a great potential for the design and synthesis of related devices.

ASSOCIATED CONTENT

Supporting Information

Photographs of color change in PVDF–DMF–CESLT solution, FT-IR spectra of different concentrations of added CESLT in PVDF films, absorption intensity due to α-, β-, and γ-phase as a function of CESLT, resonance structure of DMF and Ce(III) complex, FT-IR spectra of CESLT and CEPLX, reaction mechanism of CEPLX formation, TGA of CEPLX powder, variation of the relative electroactive phase in the PVDF composite film with CESLT loading, FT-IR spectra from 3400 to 2800 cm^{-1}, FE-SEM image of the PVF_2 film, EDS spectra PVF_2 and CEPLX–PVF_2 film, schematic circuit diagram of recording the open-circuit voltage from NG. This material is available free of charge via the Internet at http://pubs.acs.org.

AUTHOR INFORMATION

Corresponding Author

*Phone: (+91) 9433373530. E-mail: dipankar@phys.jdvu.ac.in.

Present Address

#Materials Science Centre, IIT- Kharagpur, PIN 721302, India.

Notes

The authors declare no competing financial interest.

DOI: 10.1021/am507522r
ACS Appl. Mater. Interfaces 2015, 7, 1298–1307

■ ACKNOWLEDGMENTS

This work was financially supported by a grant from the Science and Engineering Research Board (SERB/1759/2014-15), Government of India. S.G. is supported by UGC-BSR fellowship (No. P-1/RS/79/13). One of us (C.S.) thanks the CSIR, New Delhi, India, for research funding (No. 01(2731)/13/EMR-II). For help in XPS measurements we like to acknowledge G. Beuckert and M. Städter from BTU Cottbus-Senflenberg, Germany.

■ REFERENCES

(1) Cohen, Y. B.; Zhang, Q. Electroactive Polymer Actuators and Sensors. *MRS Bull.* **2008**, *33*, 173−181.
(2) Martins, P.; Lopes, A. C.; Mendeza, S. L. Electroactive Phases of Poly(vinylidene fluoride): Determination, Processing and Applications. *Prog. Polym. Sci.* **2014**, *39*, 683−706.
(3) Lovinger, A. J. Ferroelectric Polymers. *Science* **1983**, *220*, 1115−1121.
(4) Gu, L.; Cui, N.; Cheng, L.; Xu, Q.; Bai, S.; Yuan, M.; Wu, W.; Liu, J.; Zhao, Y.; Ma, F.; Qin, Y.; Wang, Z. L. Flexible Fiber Nanogenerator with 209 V Output Voltage Directly Powers a Light-Emitting Diode. *Nano Lett.* **2013**, *13*, 91−94.
(5) Mandal, D.; Yoon, S.; Kim, K. J. Origin of Piezoelectricity in an Electrospun Poly(vinylidene fluoride-trifluoroethylene) Nanofiber Web-Based Nanogenerator and Nano-Pressure Sensor. *Macromol. Rapid Commun.* **2011**, *32*, 831−837.
(6) Mandal, D.; Henkel, K.; Schmeißer, D. Improved Performance of Electrospun P(VDF-HFP) Nanofibers Based Polymer Nanogenerator Accompanied with Silver Nanoparticle Doping. *Phys. Chem. Chem. Phys.* **2014**, *16*, 10403−10407.
(7) Asadi, K.; Leeuw, D. M. D.; Boer, B.; Paul, W. M. Organic Non-Volatile Memories from Ferroelectric Phase-Separated Blends. *Nat. Mater.* **2008**, *7*, 547−550.
(8) Yang, Y.; Zhang, H.; Zhu, G.; Lee, S.; Lin, Z. H.; Wang, Z. L. Flexible Hybrid Energy Cell for Simultaneously Harvesting Thermal, Mechanical, and Solar Energies. *ACS Nano* **2012**, *7*, 785−790.
(9) Ghosh, S. K.; Alam, Md. M.; Mandal, D. The In-situ Formation of Platinum Nanoparticles and Their Catalytic Role in Electroactive Phase Formation in Poly(vinylidene fluoride): A Simple Preparation of Multifunctional poly(vinylidene fluoride) Films Doped with Platinum Nanoparticles. *RSC Adv.* **2014**, *4*, 41886−41894.
(10) Mao, Y.; Zhao, P.; McConohy, G.; Yang, H.; Tong, Y.; Wang, X. Sponge-Like Piezoelectric Polymer Films for Scalable and Integratable Nanogenerators and Self-Powered Electronic Systems. *Adv. Energy Mater.* **2014**, *4*, 1301624−1301631.
(11) Ince-Gunduz, B. S.; Alpern, R.; Amare, D.; Crawford, J.; Dolan, B.; Jones, S.; Kobylarz, R.; Reveley, M.; Cebe, P. Impact of Nanosilicates on Poly(vinylidene fluoride) Crystal Polymorphism: Part 1. Melt-Crystallization at High Supercooling. *Polymer* **2010**, *51*, 1485−1493.
(12) Mandal, D.; Henkel, K.; Schmeißer, D. The Electroactive β-Phase Formation in Poly(vinylidene fluoride) by Gold Nanoparticles Doping. *Mater. Lett.* **2012**, *73*, 123−125.
(13) Jin, J.; Zhao, F.; Han, K.; Haque, M. A.; Dong, L.; Wang, Q. Multiferroic Polymer Laminate Composites Exhibiting High Magnetoelectric Response Induced by Hydrogen-Bonding Interactions. *Adv. Funct. Mater.* **2014**, *24*, 1067−1073.
(14) Yang, Y.; Zhang, H.; Chen, J.; Lee, S.; Hou, T. C.; Wang, Z. L. Simultaneously Harvesting Mechanical and Chemical Energies by a Hybrid Cell for Self-Powered Piosensors and Personal Electronics. *Energy Environ. Sci.* **2013**, *6*, 1744−1749.
(15) Wang, Z. L. Toward Self-Powered Sensor Networks. *Nano Today* **2010**, *5*, 512−514.
(16) Li, Z.; Zhu, G.; Yang, R.; Wang, A. C.; Wang, Z. L. Muscle-Driven In Vivo Nanogenerator. *Adv. Mater.* **2010**, *22*, 2534−2537.
(17) Saravanakumar, B.; Mohan, R.; Thiyagarajan, K.; Kim, S. J. Fabrication of a ZnO Nanogenerator for Eco-Friendly Biomechanical Energy Harvesting. *RSC Adv.* **2013**, *3*, 16646−16656.
(18) Wen, X.; Yang, W.; Jing, Q.; Wang, Z. L. Harvesting Broadband Kinetic Impact Energy from Mechanical Triggering/Vibration and Water Waves. *ACS Nano* **2014**, *8*, 7405−7412.
(19) Su, Y.; Wen, X.; Zhu, G.; Yang, J.; Chen, J.; Bai, P.; Wu, Z.; Jiang, Y.; Wang, Z. L. Hybrid Triboelectric Nanogenerator for Harvesting Water Wave Energy and as a Self-Powered Distress Signal Emitter. *Nano Energy* **2014**, *9*, 186−195.
(20) Jeong, C. K.; Kim, I.; Park, K.-I.; Oh, M. H.; Paik, H.; Hwang, G.-T.; No, K.; Nam, Y. S.; Lee, K. J. Virus-Directed Design of a Flexible $BaTiO_3$ Nanogenerator. *ACS Nano* **2013**, *7*, 11016−11025.
(21) Park, K.-I.; Son, J. H.; Hwang, G.-T.; Jeong, C. K.; Ryu, J.; Koo, M.; Choi, I.; Lee, S. H.; Byun, M.; Wang, Z. L.; Lee, K. J. Highly-Efficient, Flexible Piezoelectric PZT Thin Film Nanogenerator on Plastic Substrates. *Adv. Mater.* **2014**, *26*, 2514−2520.
(22) Wu, J. M.; Xu, C.; Zhang, Y.; Yang, Y.; Zhou, Y.; Wang, Z. L. Flexible and Transparent Nanogenerators Based on a Composite of Lead-Free $ZnSnO_3$ Triangular-Belts. *Adv. Mater.* **2012**, *24*, 6094−6099.
(23) Huang, C. T.; Song, J.; Lee, W.-F.; Ding, Y.; Gao, Z.; Hao, Y.; Chen, L. J.; Wang, Z. L. GaN Nanowire Arrays for High-Output Nanogenerators. *J. Am. Chem. Soc.* **2010**, *132*, 4766−4771.
(24) Jeong, C. K.; Park, K.-I.; Ryu, J.; Hwang, G. T.; Lee, K. J. Large-Area and Flexible Lead-Free Nanocomposite Generator Using Alkaline Niobate Particles and Metal Nanorod Filler. *Adv.Funct. Mater.* **2014**, *24*, 2620−2629.
(25) Saravanakumar, B.; Soyoon, S.; Kim, S. J. Self-Powered pH Sensor Based on a Flexible Organic-Inorganic Hybrid Composite Nanogenerator. *ACS Appl. Mater. Interfaces* **2014**, *6*, 13716−13723.
(26) Cha, A.; Snyder, G. E.; Selvin, P. R.; Bezanilla, F. Atomic Scale Movement of the Voltage-Sensing Region in a Potassium Channel Measured Via Spectroscopy. *Nature* **1999**, *402*, 809−813.
(27) Montalti, M.; Prodi, L.; Zaccheroni, N.; Charbonniere, L.; Douce, L.; Ziessel, R. A Luminescent Anion Sensor Based on a Europium Hybrid Complex. *J. Am. Chem. Soc.* **2001**, *123*, 12694−12695.
(28) Zhang, J.; Badger, P. D.; Geib, S. J.; Petoud, S. Sensitization of Near-Infrared-Emitting Lanthanide Cations in Solution by Tropolonate Ligands. *Angew. Chem.* **2005**, *117*, 2564−2568.
(29) Canevali, C.; Mattoni, M.; Morazzoni, F.; Scotti, R.; Casu, M.; Musinu, A.; Krsmanovic, R.; Polizzi, S.; Speghini, A.; Bettinelli, M. Stability of Luminescent Trivalent Cerium in Silica Host Glasses Modified by Boron and Phosphorus. *J. Am. Chem. Soc.* **2005**, *127*, 14681−14691.
(30) Kaittanis, C.; Santra, S.; Asati, A.; Perez, J. M. A Cerium Oxide Nanoparticle-Based Device for the Detection of Chronic Inflammation via Optical and Magnetic Resonance Imaging. *Nanoscale* **2012**, *4*, 2117−2123.
(31) Facchetti, A.; Annoni, E.; Beverina, L.; Morone, M.; Zhu, P.; Marks, T. J.; Pagani, G. A. Very Large Electro-optic Responses in H-bonded Heteroaromatic Films Grown by Physical Vapour Deposition. *Nat. Mater.* **2004**, *3*, 910−917.
(32) Hug, S. J.; Boxer, S. G. Dipolar Character of Ligand-Centered Transitions in Transition Metal Tris-bipyridyl Complexes. *Inorg. Chim. Acta* **1996**, *242*, 323−327.
(33) Bai, P.; Zhu, G.; Zhou, Y. S.; Wang, S.; Ma, J.; Zhang, G.; Wang, Z. L. Dipole-Moment-Induced Effect on Contact Electrification for Triboelectric Nanogenerator. *Nano Res.* **2014**, DOI: 10.1007/s12274-014-0461-8.
(34) Kholkin, A. L. In *Piezoelectricity and Acoustic Materials for Transducer Applications;* Safari, A., Akdoğan, E. K., Eds.; Springer: New York, 2008; Chapter 2.
(35) Mandal, D.; Henkel, K.; Schmeisser, D. Comment on Preparation and Characterization of Silver−Poly(vinylidene fluoride) Nanocomposites: Formation of Piezoelectric Polymorph of Poly(vinylidene fluoride). *J. Phys. Chem. B* **2011**, *111*, 10567−10569.

DOI: 10.1021/am507522r
ACS Appl. Mater. Interfaces 2015, 7, 1298−1307

(36) Mandal, D.; Kim, K. J.; Lee, J. S. Simple Synthesis of Palladium Nanoparticles, β-Phase Formation, and the Control of Chain and Dipole Orientations in Palladium-Doped Poly(vinylidene fluoride) Thin Films. *Langmuir* **2012**, *28*, 10310−10317.
(37) Chen, S.; Yao, K.; Tay, F. E. H.; Liow, C. L. Ferroelectric Poly(vinylidene fluoride) Thin Films on Si Substrate with the β Phase Promoted by Hydrated Magnesium Nitrate. *J. Appl. Phys.* **2007**, *102*, 104108−104115.
(38) Samuels, R. J. *Structured Polymer Properties: The Identification, Interpretation, and Application of Crystalline Polymer Structure;* Wiley-Interscience Publication: Toronto, ON, Canada, 1974.
(39) Sarkar, S.; Garain, S.; Mandal, D.; Chattopadhyay, K. K. Electroactive Phase Formation in PVDF−BiVO4 Flexible Nanocomposite Films for High Energy Density Storage Application. *RSC Adv.* **2014**, *4*, 48220−48227.
(40) Sliozberg, Y. R.; Hoy, R. S.; Mrozek, R. A.; Lenhart, J. L.; Andzelm, J. W. Role of Entanglements and Bond Scission in High Strain-Rate Deformation of Polymer Gels. *Polymer* **2014**, *55*, 2543−2551.
(41) Silva, A. B. D.; Arjmand, M.; Sundararaj, U.; Bretas, R. E. S. Novel Composites of Copper Nanowire/PVDF with Superior Dielectric Properties. *Polymer* **2014**, *55*, 226−234.
(42) Kaminska, A.; Duzynska, A.; Berkowski, M.; Trushkin, S.; Suchocki, A. Pressure-Induced Luminescence of Cerium-Doped Gadolinium Gallium Garnet Crystal. *Phys. Rev. B* **2012**, *85*, 155111−155121.
(43) Geng, D.; Li, G.; Shang, M.; Yang, D.; Zhang, Y.; Chenga, Z.; Lin, J. J. Color Tuning via Energy Transfer in $Sr_3In(PO_4)_3$:Ce^{3+}/Tb^{3+}/Mn^{2+} Phosphors. *J. Mater. Chem.* **2012**, *22*, 14262−14271.
(44) Chall, S.; Mati, S. S.; Rakshit, S.; Bhattacharya, S. C. Soft-Templated Room Temperature Fabrication of Nanoscale Lanthanum Phosphate: Synthesis, Photoluminescence, and Energy-Transfer Behavior. *J. Phys. Chem. C* **2013**, *117*, 25146−25159.
(45) Vogler, A.; Kunkely, H. Excited State Properties of Lanthanide Complexes: Beyond ff States. *Inorg. Chim. Acta* **2006**, *359*, 4130−4138.
(46) Zheng, X. L.; Liu, Y.; Pan, M.; Qiang, X.; Zhang, J. Y.; Zhao, C. Y.; Tong, Y. X.; Su, C. Y. Bright Blue-Emitting Ce^{3+} Complexes with Encapsulating Polybenzimidazole Tripodal Ligands as Potential Electroluminescent Devices. *Angew. Chem.* **2007**, *119*, 7543−7547.
(47) Werling, K. A.; Hutchison, G. R.; Lambrecht, D. L. Piezoelectric Effects of Applied Electric Fields on Hydrogen-Bond Interactions: First-Principles Electronic Structure Investigation of Weak Electrostatic Interactions. *J. Phys. Chem. Lett.* **2013**, *4*, 1365−1370.
(48) Lee, K. Y.; Kim, D.; Lee, J. H.; Kim, T. Y.; Gupta, M. K.; Kim, S. W. Unidirectional High-Power Generation via Stress-Induced Dipole Alignment from $ZnSnO_3$ Nanocubes/Polymer Hybrid Piezoelectric Nanogenerator. *Adv. Funct. Mater.* **2013**, *24*, 37−43.

DOI: 10.1021/am507522r
ACS Appl. Mater. Interfaces 2015, 7, 1298−1307